ROYAL SOCIETY
OF CHEMISTRY

PAPER

Check for updates

An *in situ* bifacial passivation strategy for flexible perovskite solar module with mechanical robustness by roll-to-roll fabrication†

Hongyu Wang,[a] Zengqi Huang,[b] Shuqin Xiao,[a] Xiangchuan Meng,[b] Zhi Xing,[b] Li Rao,[a] Chenxiang Gong,[b] Runsheng Wu,[c] Ting Hu, [ID][ab] Licheng Tan, [ID][b] Xiaotian Hu,*[ab] Shaohua Zhang*[a] and Yiwang Chen [ID] *[bd]

The inevitable interfacial defects in the under layer of perovskite films still hinder the power conversion efficiency (PCE) and stability of perovskite solar cells (PSCs), especially of large-area flexible devices up-scaled by roll-to-roll (R2R) technology. Herein, we demonstrate an *in situ* bifacial passivation strategy *via* a simple hydroiodic acid (HI) soaking of NiO_x-based hole transport layer during R2R printing. Concretely, the trivalent nickel compound on the film surface is reduced to nickel iodide (NiI_2) by a HI redox reaction, thereby optimizing the interface contact and ameliorating the work function. Meanwhile, NiI_2 coordinates with lead atoms in the perovskite to form a Pb−I bond, which induces the orderly growth of the perovskite lattice and enhances the quality of the crystalline film. Consequently, the PCE of the optimized flexible devices reaches up to 19.04% (1 cm^2) and 16.15% (15 cm^2). Moreover, the stability and mechanical property of these devices are also improved. This work provides a deep understanding of the NiO_x/perovskite interface and an approach for printable interface optimization.

Introduction

In recent years, organic–inorganic halide perovskite solar cells have been developed rapidly as next-generation photovoltaic devices, owing to the rapid improvement in efficiency (over 25%) and long-time stability of PSCs.[1-4] Specifically, flexible devices have been extensively studied for their wide application prospects, which has enabled portability and roll-to-roll (R2R) fabrication to be implemented in large-area modules.[5-7] Meanwhile, due to the low-temperature processability and efficient photogenerated carrier separation, p–i–n planar structure has been generally adopted in flexible PSCs.[8,9] However, there still exist some problems in large-scale flexible PSCs, such as the brittleness of indium tin oxide (ITO) electrode and poor film morphology of the charge transport layer and perovskite layer,[10,11] which could significantly reduce the device performance. Up to now, although some PEDOT:PSS electrodes have been developed into large-area flexible PSCs,[10,12-16] the work

function of these alternatives does not match well with that of the perovskite layer, leading a relatively low open-circuit voltage (V_{oc}).[17-20] Thus, a hole transport layer (HTL) is urgently needed to modify the PEDOT:PSS electrode with suitable energy level alignment. Meanwhile, the hole transport layer sandwiched between the photoactive perovskite and charge collection electrode plays a significant role in improving device performance by promoting perovskite crystal growth and optimizing carrier transport.[21-24]

In general, the most widely used hole transport materials in p–i–n flexible perovskite devices are mainly poly (3,4-ethylenedioxythiophene):polystyrene sulfonate (PEDOT:PSS) Al4083,[25] poly[bis(4-phenyl)(2,4,6-trimethylphenyl)amine] (PTAA)[26] and NiO_x.[27] However, as organic HTLs, PEDOT:PSS Al4083 and PTAA possess several drawbacks, such as mismatched work function, high cost, and easy degradation in humidity and air.[28] These inherent disadvantages limit their application in the R2R production.[28,29] By contrast, low-temperature-processed NiO_x is regarded as a promising HTL candidate with the superiorities of wide-bandgap, good optical transparency, excellent stability and low cost.[30,31] However, due to the poor printability of NiO_x and the enrichment of Ni^{3+} compounds on the surface,[32,33] there usually exist many defects on the film surface, which incur hole accumulation near the perovskite interface with trap-assisted nonradiative recombination losses.[34] In addition, these defects lead to a rough contact with the perovskite layer, which deteriorates the film morphology and generates more interface defects.[35,36] In order

[a] School of Materials Science and Engineering, Nanchang University, 999 Xuefu Avenue, Nanchang 330031, China. E-mail: shz@ncu.edu.cn; happyhu@ncu.edu.cn

[b] College of Chemistry, Institute of Polymers and Energy Chemistry, Nanchang University, Nanchang 330031, P. R. China. E-mail: ywchen@ncu.edu.cn

[c] School of New Energy Science and Engineering, Xinyu University, Xinyu 338004, China

[d] Institute of Advanced Scientific Research (iASR), Jiangxi Normal University, 99 Ziyang Avenue, Nanchang 330022, China

† Electronic supplementary information (ESI) available. See DOI: 10.1039/d0ta12067g

This journal is © The Royal Society of Chemistry 2021

J. Mater. Chem. A, 2021, 9, 5759–5768 | 5759

to solve the above issues, He *et al.* applied potassium chloride (KCl) to modify the surface of the NiO_x film to improve the ordering of the perovskite crystals at the interface, thereby reducing interface defects and inhibiting charge recombination.[37] Park *et al.* improved the interface contact and passivated interface defects by inserting an organic interlayer between the NiO_x and perovskite layers.[38] These results indicate that controlling the interface between the NiO_x HTL and the perovskite photoactive layer is an effective strategy to passivate interface defects. Due to the complexity of these processes, the application in large-area printing has not been effectively confirmed. Therefore, it is very important to develop an interface passivation technology for large-area printing.

In this work, we demonstrate a simple bifacial passivation strategy at the NiO_x-perovskite interface during the R2R printing process. As shown in Fig. 1a, due to the acidity and reducibility of hydroiodic acid (HI), an *in situ* soaking treatment is performed. The content of Ni^{3+} compounds enriched on the surface of the NiO_x film is greatly reduced, which simultaneously decreases the interface defects and adjusts the work function of NiO_x. Meanwhile, the iodide ions (I^-) in the reaction product nickel iodide (NiI_2) form I–Pb bonds with lead in the perovskite lattice to effectively passivate the I^- vacancy defects in the perovskite. Perovskite films with low defects can effectively inhibit interfacial charge recombination and improve charge transfer. With the assistance of the HI treatment and solution shearing during the printing process, flexible perovskite solar cells are fabricated with a champion power

conversion efficiency (PCE) of 19.04% (1.01 cm^2). Moreover, a 15 cm^2 HI-treated PSC module is successfully fabricated *via* R2R printing (Fig. 1b), which shows a PCE of 16.15% on a flexible substrate with remarkable environmental stability and mechanical robustness. This work provides a new strategy for interface optimization, which provides significant inspiration for the fabrication of high-performance flexible PSCs.

Results and discussion

To validate the multiple effects of this *in situ* bifacial passivation, 1.01 cm^2 rigid perovskite devices are firstly fabricated by meniscus-coating (Fig. S1, ESI†) with a structure of glass/hc-PEDOT:PSS[10]/NiO_x/perovskite/$PC_{61}BM$/Ag. During the fabrication of NiO_x films, NiO_x nanoparticles are induced to evenly deposit on the substrate owing to the shear force of the solution, which could greatly optimize the morphology of the NiO_x films as compared with the preparation by spin coating. To further confirm the above theory, atomic force microscopy (AFM) (Fig. S2, ESI†) and optical microscopy (OM) (Fig. S3 and S4, ESI†) characterizations of NiO_x films fabricated by the meniscus-coating process and spin-coating process are carried out. The results show that the NiO_x films fabricated by the meniscus-coating process are more uniform and there is no obvious aggregation phenomenon. Then, the meniscus-coated NiO_x films are treated with HI solution, and the device performance is greatly enhanced from 17.86% (reference) to 20.51% (HI treatment) (Fig. S5, ESI†). Subsequently, the meniscus-
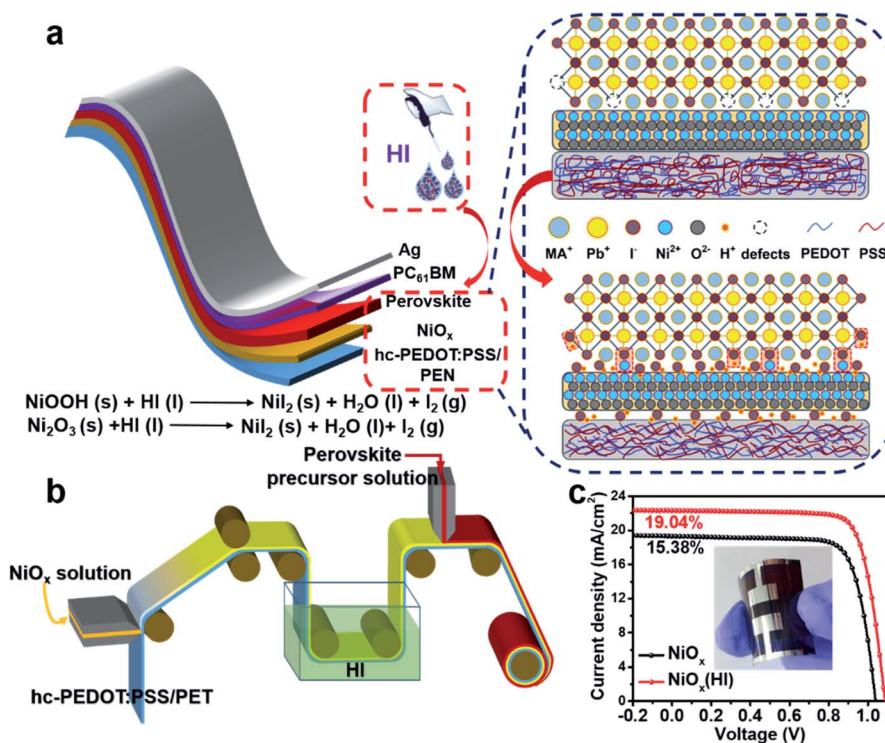

Fig. 1 *In situ* bifacial passivation mechanism and device preparation. (a) Diagram of the passivation mechanism. (b) Fabrication procedure for perovskite solar cells by R2R process. (c) *J*–*V* curves of flexible devices (1.01 cm^2) with and without HI treatment. Inset presents the photograph of flexible perovskite solar cells.

coated prototype is extended to the flexible R2R printing system. The R2R printing has been proved to be a mature technology for fabricating large-scale flexible devices.[39–43] Thus, we have used the R2R printing technology for further fabricating flexible PSCs.
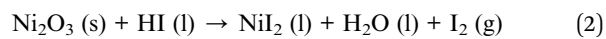
Before R2R printing, the optimal concentration for HI surface modification needs to be explored to maximize device performance. The *in situ* soaking treatment with HI at concentrations of 0.1 wt%, 0.3 wt%, 0.6 wt% and 0.9 wt%, respectively, is further investigated. The typical *J–V* curves of the devices with different concentrations of HI soaking treatment are shown in Fig. S6 (ESI†), and the corresponding photovoltaic parameters are summarized in Table S1 (ESI†). The PCE increases significantly with a maximum performance attained when the perovskite films are soaked in a 0.6 wt% HI solution. The device performance begins to drop when the HI concentration further increases to 0.9 wt%, possibly owing to excessive reduction caused by HI. The best PCE of 19.04% for the flexible devices (1.01 cm^2) is achieved with 0.6 wt% HI surface treatment under 1-sun condition, along with a V_{oc} as high as 1.09 V, a short-circuit current density (J_{sc}) of 22.32 mA cm^{-2} and a fill factor (FF) of 78.26%, that is much higher than 15.38% without HI treatment (Fig. 1c). Therefore, the optimal concentration for HI treatment is defined as 0.6 wt% for the following characterizations.

Effects of HI treatment on NiO$_x$ film

To directly investigate the changes in the NiO$_x$ films after HI treatment, X-ray photoelectron spectroscopy (XPS) analysis is performed to explore the element composition of the NiO$_x$ films. The Ni 2p$_{3/2}$ characteristic peaks of the NiO$_x$ film are shown in Fig. 2a. The background is subtracted from the XPS spectra by using a Shirley-type background subtraction. The fractional peak of the XPS spectrum demonstrates that the Ni 2p spectrum could be well fitted by two different valence states (Ni^{2+} and Ni^{3+}) in the form of a Gaussian function. Whether in modified or unmodified NiO$_x$ films, the remarkable contributor peaks of the Ni^{3+} state such as in NiOOH (Ni 2p$_{3/2}$ at 856.0 eV) and Ni$_2$O$_3$ (Ni 2p$_{3/2}$ at 855.0 eV) and the Ni^{2+} state as in NiO (Ni 2p$_{3/2}$ at 853.7 eV) are observed,[44–47] which illustrates that the composition of the NiO$_x$ film is nonstoichiometric. However, it is important to mention that these Ni^{3+} state compounds (NiOOH, Ni$_2$O$_3$) can reduce the work function and the transmittance of the NiO$_x$ film,[48–50] which can greatly degrade its photovoltaic performance. Nevertheless, after the HI treatment on the NiO$_x$ film, the compositions of the film are significantly changed, thereby optimizing the film characteristics. Obviously, the characteristic peak area of the Ni^{3+} state is decreased and that of the Ni^{2+} state is increased after the HI treatment. As calculated from the integral area in the Ni$_{2p}$ spectrum, the obtained ratio of Ni^{3+}/Ni^{2+} changes from 3 : 2 to 1 : 1, which indicates that HI interacts with the Ni^{3+} compounds on the surface of NiO$_x$ films.

In order to determine the chemical reaction on the surface of the NiO$_x$ films treated with HI solution, Gibbs free energy (ΔG) calculation is carried out to judge the progress of the reaction. The corresponding chemical reaction equations in this process are shown as follows:

$$Ni(OH)_2 \ (s) + HI \ (l) \rightarrow NiI_2 \ (l) + H_2O \ (l) \tag{1}$$

$$Ni_2O_3 \ (s) + HI \ (l) \rightarrow NiI_2 \ (l) + H_2O \ (l) + I_2 \ (g) \tag{2}$$

According to the formula $\Delta G = \Delta H - T\Delta S$, the ΔG of the above reactions are all less than zero, which indicates that the reaction is spontaneous (see detailed explanations about Gibbs free energy calculation of reaction equations in ESI Note 1†).
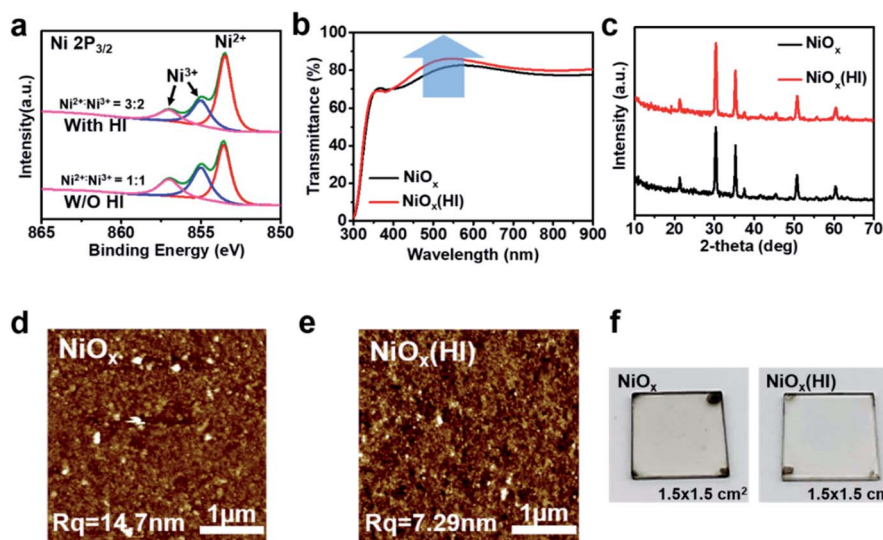

Fig. 2 Interface modification of NiO$_x$ by HI treatment. (a) High-resolution X-ray photoelectron spectroscopy (XPS) spectra of Ni in the NiO$_x$ and NiO$_x$ (HI) films. (b) Transmittance spectra of the corresponding NiO$_x$ films. (c) X-ray diffraction (XRD) patterns of NiO$_x$ film with and without HI treatment. (d and e) The atomic force microscopy (AFM) images of NiO$_x$ film with and without HI modification. (f) The photographs of the corresponding NiO$_x$ films.

This journal is © The Royal Society of Chemistry 2021

J. Mater. Chem. A, 2021, **9**, 5759–5768 | **5761**

The reduction of Ni^{3+} compounds in the NiO_x films is beneficial to increase the work function of NiO_x, which helps to achieve better energy alignment.[51] As illustrated in Fig. S7,† the energy levels of the NiO_x films with or without HI surface modification are measured with ultraviolet photoelectron spectroscopy (UPS) and the corresponding energy level diagrams of PSCs are drawn. The valence band maximum (VBM) values can be calculated according to the formula $VBM = W_F + (E_F - E_{VB})$, where W_F is the work function, E_F is the Fermi level, and E_{VB} is the valence band energy level.[52] The VBM energy (5.34 eV) of the NiO_x film with HI surface modification is more aligned with the valence band (5.47 eV) of the perovskite, which is beneficial for hole transporting and electron blocking. To further explore the electrical properties of the NiO_x film, the electrical conductivity and surface electrostatic potential are measured. As shown in Fig. S8,† the conductivity of the NiO_x film after HI acid surface treatment has been slightly increased from 2.30×10^{-4} S m^{-1} to 2.84×10^{-4} S m^{-1}, which is beneficial to enhance carrier transport and increase the open circuit voltage. Moreover, the surface potential of the NiO_x film is measured by Kelvin probe force microscopy (KPFM).

As shown in Fig. S9,† the surface potential of the NiO_x film with HI treatment is smaller than that of pristine NiO_x film, indicating that the HI surface modification treatment slightly increases the work function of NiO_x. This is consistent with the UPS results. Meanwhile, the NiO_x films exhibit higher light transmittance in the visible spectrum after HI surface treatment due to the decrease in hydroxides on the surface of the NiO_x films. Hydroxyl (–OH) groups are mainly distributed on the surface of the NiO_x film to induce interface defects.[36,53] As shown in Fig. 2b, the transmittance of PET/hc-PEDOT:PSS/NiO_x substrate can be significantly improved in the visible light range after HI surface treatment, which is conducive to enhancing the absorption of photons in the perovskite layer. In addition, since the as-prepared NiO_x films are deposited *via* NiO_x nanoparticles, the HI interface modification does not affect the

crystallization of NiO_x, which can be confirmed by the X-ray diffraction (XRD) patterns (Fig. 2c). From the diffraction pattern, the NiO_x is a cubic crystal structure and there is no significant difference in the characteristic peaks before and after HI treatment.

To investigate the changes in NiO_x film morphology after HI treatment, the morphology of the NiO_x films is examined by using atomic force microscopy (AFM). As shown in Fig. 2d and e, although the NiO_x nanoparticles are very small and uniform, the roughness of both NiO_x and NiO_x (HI) films is still quite large. This may be caused by the easy aggregation of nanoparticles, and this aggregation phenomenon becomes more serious as the printing area increases. However, the NiO_x film based on HI surface treatment presents a smooth surface roughness, which could be attributed to the reduction of the surface defect state induced by the hydroxyl (–OH).[53] In addition, such a smooth surface is beneficial to reduce the trap state of the interface and enhance the ohmic contact between layers. This result is consistent with the previous analysis. The photographs, as shown in Fig. 2f, further prove that the NiO_x film with HI surface treatment is more transparent and smoother, which contributes to improving the light transmittance of the film as well as optimizing the interface contact.

Effects of HI treatment on perovskite film

In addition, for the purpose of exploring whether the interface products can interact with the upper perovskite layer, charge differential density analysis and *ab initio* molecular dynamics (AIMD) simulation are performed on the interface between NiO_x and perovskite layers.[54] According to the charge density analysis (Fig. 3a and S10†), the reaction product nickel iodide (NiI_2) existing at the interface can interact with the perovskite crystals, resulting in the redistribution of interface charges. As illustrated in Fig. 3a, the charge density of I and Pb element at the interface increases, indicating that the Pb–I bond is formed at the interface. From partial charge density analysis (Fig. 3a), the
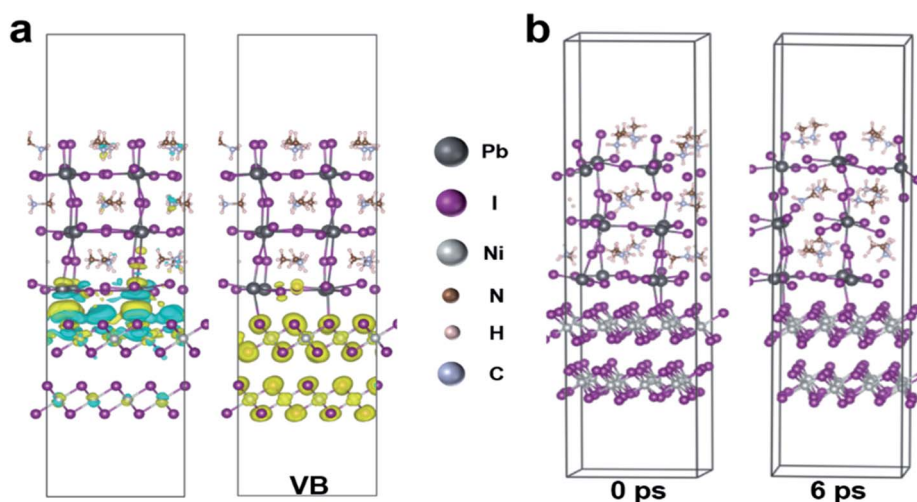

Fig. 3 The Interface interaction between NiO_x (HI) and perovskite films. (a) Charge differential density analysis of the interfaces. (b) *Ab initio* molecular dynamics (AIMD) of the interaction between NiI_2 and perovskite. For simplifying the calculation, $MAPbI_3$ perovskite supercell is used for AIMD simulation.

5762 | *J. Mater. Chem. A*, 2021, **9**, 5759–5768

This journal is © The Royal Society of Chemistry 2021

valence band below the Fermi level is mainly distributed on NiI_2, whereas the conduction band above the Fermi level is mainly distributed on the perovskite. Then, AIMD simulation is employed to analyze the stable existence of I–Pb bonds. The simulation model we have chosen is the interface between NiO_x (HI) (HI-modified NiO_x) and perovskite (001) film, and the system dynamics are evolved at 300 K for several picoseconds. As shown in Fig. 3b, the structure can remain stable at 300 K during the simulation (after 6 ps) without significant distortion of the geometric structure, indicating the high thermodynamic stability of NiI_2/perovskite. The potential energy and the temperature are also oscillating near the equilibrium state (Fig. S11†). The first peak of the radical distribution function (RDF) of Ni–I (Fig. S12†) is at 2.72 Å. There is no distribution between the first and second peak, which indicates stable Ni–I bonds. The first peak of RDF of Pb–I (Fig. S12†) is at 3.07 Å, but Pb–I is not always kept stable at the interface. As shown in Fig. S13,† the Pb–I bond length fluctuates between 3.5 to 5 Å, which results in a dynamic equilibrium at the interface. Obviously, the stable I–Pb bond formed at the interface can stabilize the perovskite lattice and inhibit the decomposition of the perovskite and the formation of vacancy defects, which is beneficial to reduce the defect states of the interface to facilitate the extraction and transport of charge carriers, thereby optimizing the photovoltaic performance of the flexible device.

In order to further detect the influence of this interaction effect on the perovskite film, the resulted perovskite films deposited on different NiO_x films are characterized. The perovskite films are deposited by using a continuous R2R process and sequentially annealed at 100 °C for 30 min in a low dew point condition. The cross-section scanning electron microscopy (SEM) and atomic force microscopy (AFM) are conducted to investigate the effect of NiI_2 on the perovskite film morphology and quality. As shown in Fig. 4a and S14,† a high-quality perovskite film composed of large grains and super-compact device structure is obtained upon the NiO_x film with HI treatment, while the reference perovskite film exhibits small grains with more grain boundaries. More interestingly, the optimized perovskite crystal growth has an obvious vertical orientation. The average grain size of the perovskite films is increased from 185 nm to 336 nm after HI interface treatment (Fig. S15, ESI†), which could be ascribed to the influence of the formation of Pb–I bond on perovskite crystallization at the interface. The formation of Pb–I bond at the interface helps to induce the nucleation and directional growth of the perovskite at the interface, which leads to an increase in the size of the perovskite grains and the formation of dense perovskite films with high crystallinity.[54] In order to further explore the crystal growth of the corresponding perovskite films, 2D grazing-incidence wide-angle X-ray scattering (GIWAXS) is measured to study the crystal characteristics of the perovskite films. As shown in Fig. 4b, the (110) diffraction peak of the perovskite based on NiO_x (HI) layer is significantly enhanced as compared with that of the control film, which corresponds with the results of XRD measurements (Fig. S16, ESI†). In addition, the standard diffraction peak intensity of PbI_2 at $2\theta = 12.67°$ is missing in the
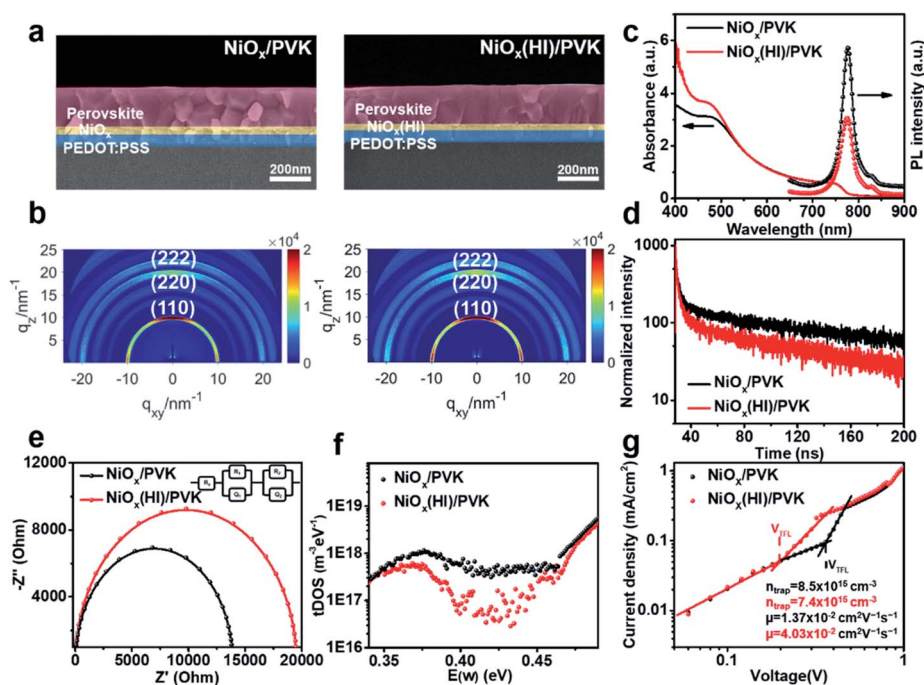

Fig. 4 Crystallization and quality of flexible perovskite films based on the NiO_x films with and without HI treatment. (a) Cross-section SEM images of the PEDOT:PSS/NiO_x/PVK layers. (b) 2D GIWAXS scattering patterns for the corresponding perovskite films. (c) UV-vis absorption spectra and steady-state PL spectra of the corresponding perovskite films. (d) Time-resolved photoluminescence (TRPL) of perovskite films. (e) The typical Nyquist plots of the corresponding PSCs. (f) Trap density of states (tDOS) spectra for the corresponding PSCs. (g) The space-charge-limited-current (SCLC) module for NiO_x and NiO_x (HI) hole-only devices.

perovskite film based on NiO$_x$ (HI) layer, which indicates that the formation of I–Pb bonds at the interface can effectively improve the quality of the perovskite film and inhibit the degradation of the perovskite.[55] Meanwhile, the optimized perovskite film also helps to improve the photon collection of the flexible devices, which leads to a stronger absorption in the UV-vis spectra (Fig. 4c). Steady-state photoluminescence (PL) and time-resolved photoluminescence (TRPL) spectroscopy measurements are further employed to investigate the effect of NiI$_2$ defect passivation on the carrier dynamics at the interface. As shown in Fig. 4c, the lower fluorescence intensity of the samples based on NiO$_x$ (HI) layer indicates that the charge carriers are effectively extracted and the non-radiative recombination loss at the interface is significantly reduced. Similar results are revealed in the TRPL spectra (see in Fig. 4d). The perovskite films based on NiO$_x$ (HI) layer yield a shorter carrier recombination lifetime than the reference (23 ns versus 35 ns). These results could indicate that the photogenerated hole from the perovskite layer can be effectively extracted and transferred to the anode with an ideal ohmic contact.[56] More importantly, the significant decrease observed in the PL intensity and TRPL decay time could be caused by the passivation of interface defects. In general, the deep-level defects at the surface of polycrystalline perovskite films, such as iodine vacancies, could become the non-radiative recombination centers of charge carriers. These defects may result in V_{oc} losses,[57,58] which will reduce the device performance. Interestingly, the excess iodide

ions remaining at the interface can effectively fill in the iodine vacancy by HI treatment, thereby passivating perovskite interface defects and suppressing non-radiative carrier recombination.

To better understand the charge carrier recombination and the distribution of defects, the electrochemical impedance spectroscopy (EIS) of the corresponding devices with an applied potential of 0.8 V under dark conditions over a frequency range of 100 MHz to 4 MHz is conducted. The Nyquist plots for the devices with and without HI interface treatment are shown in Fig. 4e. The larger semicircle corresponding to the devices with HI interface treatment demonstrates a larger recombination resistance, which indicates a lower carrier recombination rate due to the in situ bifacial passivation of NiI$_2$. Furthermore, the carrier trap density and mobility of various perovskite films are also explored. Fig. 4f describes that the devices based on NiO$_x$ (HI) layer have lower trap density of states (tDOS) almost over the whole trap depth region, which confirms the beneficial role of HI interface treatment in reducing the deep defects. The I–V response of the crystals in the space-charge-limited-current (SCLC) regime is also measured (Fig. 4g). According to the characteristic I–V trace, the carrier trap density of the device based on HI-treated NiO$_x$ layer is calculated to be about 7.4 × 10^{15} cm^{-3}, which is much lower than that of the reference device (about 8.5 × 10^{15} cm^{-3}). The carrier mobility shows a similar trend, which increases from 1.37 × 10^{-2} cm^2 V^{-1} s^{-1} to 4.03 × 10^{-2} cm^2 V^{-1} s^{-1}. These results are consistent with the
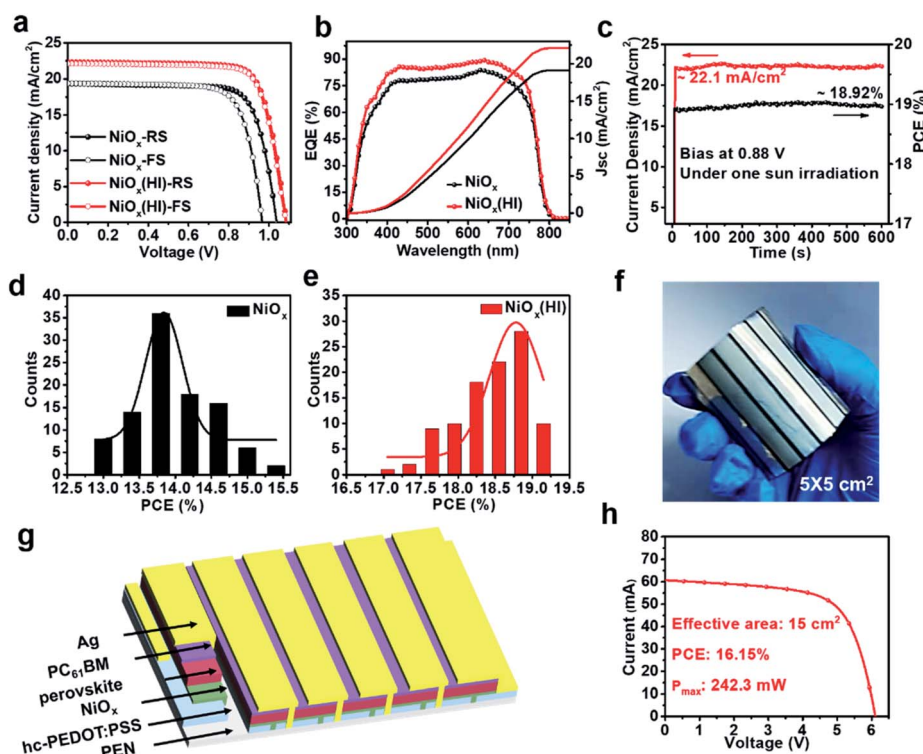

Fig. 5 Device performance of PSCs based on NiO$_x$ and NiO$_x$ (HI) HTLs. (a) J–V curves of flexible PSCs measured in the reverse and forward directions. (b) EQE spectra and integrated J_{sc} curves of flexible PSCs. (c) Steady-state PCE and current of flexible PSCs at the voltage near the maximum power point. (d and e) Performance distribution of the flexible PSCs. (f) Photograph of the flexible perovskite solar module. (g) The structure of the six section series connected large-area flexible PSCMs. (h) I–V curve of the flexible module based on NiO$_x$ (HI) HTL.

5764 | J. Mater. Chem. A, 2021, **9**, 5759–5768

This journal is © The Royal Society of Chemistry 2021

previous analysis. The efficient charge extraction and transfer, as well as fewer interface defects, are mainly derived from the high-quality perovskite films and *in situ* bifacial passivation of NiI_2 at the interface.

Characterization of device performance and module design

To validate the influence of the *in situ* bifacial passivation strategy on photovoltaic performance, the hysteresis phenomenon is then studied. As shown in Fig. 5a and Table S1,† the pristine device exhibits a typical *J–V* hysteresis, where inferior PCEs of 15.38% and 14.15% appear in forward scan (FS) and reverse scan (RS), respectively. By contrast, champion PCEs of 19.04% (RS) and 18.80% (FS) are obtained for the HI-treated devices, which shows negligible hysteresis. Moreover, the corresponding external quantum efficiency (EQE) spectra (Fig. 5a) of these champion devices exhibit an improvement in the integration current. The corresponding integrated J_{sc} is in good agreement with the value obtained from the *J–V* curves. To further describe the continuous output of the HI-treated devices, stabilized photocurrent is measured at a bias voltage of 0.88 V. These devices deliver a stabilized photocurrent of 22.1

mA cm^{-2} and a stabilized output power of 18.92% after 600 s of continuous irradiation (Fig. 5c). Besides, 100 samples for each device are fabricated to explore the efficiency and reproducibility. The efficiency histogram is combined with the Gaussian fitting. As illustrated in Fig. 5d and e, the devices based on HI treatment show favourable reliability with narrower PCE distribution, and the averaged PCE shows an obvious enhancement from 14.20% (reference) to 18.50% (HI treatment). The satisfactory performance and reproducibility can be attributed to the defect passivation of NiI_2 and high-quality PVK films. Furthermore, in order to prove that the defect passivation of NiI_2 inhibits carrier recombination at the interface, the dark current voltage characteristics of the corresponding devices are measured. As shown in Fig. S17 (ESI†), the device based on HI treatment has a lower dark current density, which suggests that more photogenerated carriers can be efficiently transmitted instead of direct shunting, resulting in suppressed charge carrier recombination and leakage current.[59,60] In addition, the details of carrier recombination are further investigated by measuring the *J–V* curves under various illumination intensities (see in Fig. S18, ESI†). The interface recombination of devices based on HI treatment is significantly reduced, which is
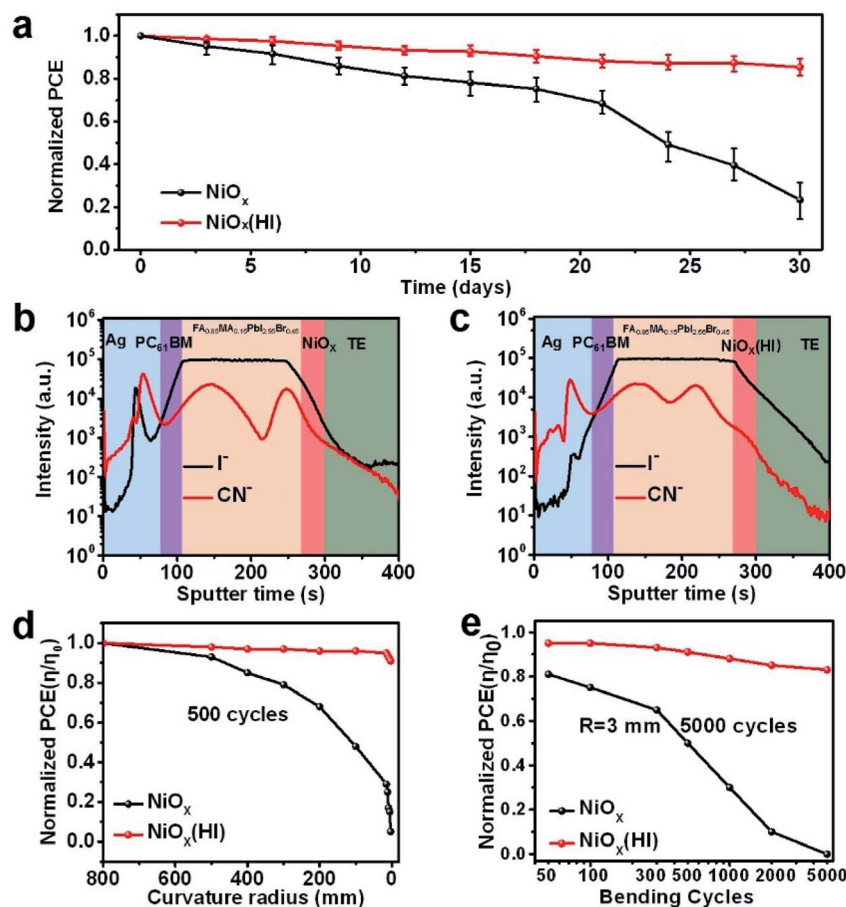

Fig. 6 Stability evaluation of large-area flexible module. (a) Normalized PCE of encapsulated PSCs based on NiO_x and NiO_x (HI) hole-transport layers under ambient condition (25–55% relative humidity and 25–35 °C) for 30 days. ToF-SIMS elemental depth profiles of devices based on (b) NiO_x and (c) NiO_x (HI) hole-transport layers. (d) Normalized averaged PCE of flexible PSCs chips measured after 500 bending cycles within a curvature radius. (e) Normalized averaged PCE of PSC chips as a function of bending cycles with radius of 3 mm.

This journal is © The Royal Society of Chemistry 2021

J. Mater. Chem. A, 2021, **9**, 5759–5768 | **5765**

consistent with the above analysis. These results indicate that HI interface treatment can reduce trap-assisted and bimolecular recombination due to the improvement in the perovskite film quality and interfacial contact. In view of the excellent performance of small-area flexible devices, the large-area module based on R2R printing is designed, the corresponding photograph and device structure are shown in the Fig. 5f and g, respectively. The 5×5 cm^2 module is composed of six sub-cells in series (see in Fig. S19†), which occupies an effective area of 15 cm^2 (Fig. S20†). The $I–V$ curve of the flexible module based on NiO$_x$ (HI) is shown in Fig. 5h with a high PCE of 16.15% and a maximum power of 242.3 mW. More importantly, the HI interface treatment is compatible with R2R printing, thereby realizing a continuous printing process.

Long-term and mechanical stability of the flexible devices

According to literature reports, perovskite devices suffer from severe degradation during operation due to external environmental pressures,[60] and this process is usually fatal to the stability of large-area modules. Thus, we have systematically examined the unencapsulated module with and without HI treatment to help understand the operational stability. As presented in Fig. 6a, the long-term stability of the corresponding flexible modules has been evaluated. These modules are stored in air conditions (relative humidity of 30% and 25 °C) without encapsulation. The HI-treated devices exhibit excellent stability; they retain over 80% of the original PCE value after 30 days of degradation. In contrast, the devices without HI treatment maintain only 30% of the initial efficiency. The enhancement of device stability could benefit from the *in situ* bifacial passivation of NiI$_2$ and the compact perovskite film with fewer grain boundaries, which could effectively suppress device degradation caused by ion migration. To further explore the mechanism of degradation inside the device, time-of-flight secondary ion mass spectroscopy (ToF-SIMS) is employed to detect elemental distribution with aging time. The depth profiles of the reference and the HI-treated devices after storage in ambient conditions for 30 days are shown in Fig. 6b and c, respectively. The I$^-$ ions of the devices without HI treatment diffuse obviously much deeper into the NiO$_x$ and top silver electrode than those of the devices based on HI treatment. This result further suggests that fewer interface defects and optimized perovskite films are beneficial to inhibit the migration of iodide ions between layers. In addition, the mechanical stability of flexible devices is studied by bending at various curvature radii (from flat to 3 mm). The bending photos of flexible devices under different bending radii are shown in Fig. S21.† As shown in Fig. 6d, the comparison demonstrates that the HI-treated flexible devices exhibit a better bending resistance after 500 bending cycles, which maintain over 80% of the original PCE value under a 3 mm bending radius. Moreover, the normalized PCE for the corresponding devices with different bending cycles at a bending radius of 3 mm is measured, as presented in Fig. 6e. After 5000 bending cycles, the devices based on the HI-treated NiO$_x$ layers still retain more than 80% of the original PCE value, but the reference devices are damaged, which correspond

with the SEM image analysis (Fig. S22†). These evidences show that the HI interface treatment can effectively improve the mechanical stability of the device, which is mainly attributed to the fact that *in situ* bifacial passivation of NiI$_2$ reduces the intrinsic stress caused by defects in the film.

Conclusions

In summary, the maximized collocation between NiO$_x$ and perovskite has been realized *via* HI interface treatment. The introduction of HI treatment can effectively reduce the trivalent compounds to NiI$_2$ on the surface of NiO$_x$ films, thereby increasing the work function of NiO$_x$ and passivating the surface defects. At the same time, the iodine in the reaction product NiI$_2$ can coordinate with the lead in the perovskite to passivate deep-level defects and stabilize the perovskite lattice, thereby reducing the interface defect states and inhibiting the recombination of carriers. The formation of Pb–I bonds at the interface can induce the orderly growth of perovskite grains, thereby increasing the grain size and optimizing the morphology of the film. Better level matching, fewer interface defects, and high-quality perovskite films result in high-performance flexible perovskite devices. Finally, we have fabricated flexible devices by R2R printing and have achieved a high PCE of 19.04% for 1.01 cm^2 flexible PSCs and 16.15% for a 15 cm^2 solar module with negligible hysteresis. These flexible devices also present excellent bending resistance and long-term stability. The positive effects brought by the HI treatment are promising for pursuing high-performance and stable large area perovskite solar cell modules. This strategy provides an effective approach for the future development of scalable perovskite electronics.

Author contributions

Y. C., X. H. and S. Z. conceived and designed the experiments. H. W., Z. H. and S. X. contributed equally to this work. H. W., Z. H. and X. M. fabricated the devices and measured the photovoltaic parameters. Z. X., S. X. and R. W. conducted the finite element simulation. L. R. and C. G. conducted the AFM measurements. L. T. and H. W. carried out the spectrum analysis. H. W., X. H. and Y. C. wrote the manuscript. All authors contributed to the data analysis, discussed the results and commented on the manuscript.

Conflicts of interest

There are no conflicts to declare.

Acknowledgements

5766 | *J. Mater. Chem. A*, 2021, **9**, 5759–5768

This journal is © The Royal Society of Chemistry 2021

Notes and references

1 Q. Dong, Y. Fang, Y. Shao, P. Mulligan, J. Qiu, L. Cao and J. Huang, *Science*, 2015, **347**, 967–970.

2 H. Zhou, Q. Chen, G. Li, S. Luo, T. Song, H. Duan, Z. Hong, J. You, Y. Liu and Y. Yang, *Science*, 2014, **345**, 542–546.

3 H. Chen, T. Liu, P. Zhou, S. Li, J. Ren, H. He, J. Wang, N. Wang and S. Guo, *Adv. Mater.*, 2019, **32**, 1905661.

4 K. Huang, Y. Peng, Y. Gao, J. Shi, H. Li, X. Mo, H. Huang, Y. Gao, L. Ding and J. Yang, *Adv. Energy Mater.*, 2019, **9**, 1901419.

5 T. Bu, J. Li, F. Zheng, W. Chen, X. Wen, Z. Ku, Y. Peng, J. Zhong, Y. Cheng and F. Huang, *Nat. Commun.*, 2018, **9**, 4609.

6 Y. Y. Kim, T. Yang, R. Suhonen, M. Välimäki, T. Maaninen, A. Kemppainen, N. J. Jeon and J. Seo, *Adv. Sci.*, 2019, **6**, 1802094.

7 J. Kim, S. Kim, C. Zuo, M. Gao, D. Vak and D. Y. Kim, *Adv. Funct. Mater.*, 2019, **29**, 1809194.

8 H. Chen, Q. Wei, M. I. Saidaminov, F. Wang, A. Johnston, Y. Hou, Z. Peng, K. Xu, W. Zhou, Z. Liu, L. Qiao, X. Wang, S. Xu, J. Li, R. Long, Y. Ke, E. H. Sargent and Z. Ning, *Adv. Mater.*, 2019, **31**, 1903559.

9 Q. Xue, M. Liu, Z. Li, L. Yan, Z. Hu, J. Zhou, W. Li, X. Jiang, B. Xu, F. Huang, Y. Li, H.-L. Yip and Y. Cao, *Adv. Funct. Mater.*, 2018, **28**, 1707444.

10 X. Hu, X. Meng, L. Zhang, Y. Zhang, Z. Cai, Z. Huang, M. Su, Y. Wang, M. Li, F. Li, X. Yao, F. Wang, W. Ma, Y. Chen and Y. Song, *Joule*, 2019, **3**, 1–14.

11 Z. Liu, S. Li, X. Wang, Y. Cui, Y. Qin, S. Leng, Y. Xu, K. Yao and H. Huang, *Nano Energy*, 2019, **62**, 734.

12 X. Fan, W. Nie, H. Tsai, N. Wang, H. Huang, Y. Cheng, R. Wen, L. Ma, F. Yan and Y. Xia, *Adv. Sci.*, 2019, **6**, 1900813.

13 Y. Xia, K. Sun and J. Ouyang, *Adv. Mater.*, 2012, **24**, 2436.

14 N. Kim, S. Kee, S. H. Lee, B. H. Lee, Y. H. Kahng, Y.-R. Jo, B.-J. Kim and K. Lee, *Adv. Mater.*, 2014, **26**, 2268.

15 N. Kim, H. Kang, J.-H. Lee, S. Kee, S. H. Lee and K. Lee, *Adv. Mater.*, 2015, **27**, 2317.

16 X. Fan, B. Xu, S. Liu, C. Cui, J. Wang and F. Yan, *ACS Appl. Mater. Interfaces*, 2016, **8**, 14029.

17 Y. Zhang, L. Chen, X. Hu, L. Zhang and Y. Chen, *Sci. Rep.*, 2015, **5**, 12839.

18 X. Hu, Z. Huang, X. Zhou, P. Li, Y. Wang, Z. Huang, M. Su, W. Ren, F. Li, M. Li, Y. Chen and Y. Song, *Adv. Mater.*, 2017, **29**, 1703236.

19 S. Allard, M. Forster, B. Souharce, H. Thiem and U. Scherf, *Angew. Chem., Int. Ed.*, 2008, **47**, 4070.

20 C. Zuo and L. Ding, *Adv. Energy Mater.*, 2017, **7**, 1601193.

21 C. Shen, Y. Wu, H. Zhang, E. Li, W. Zhang, X. Xu, W. Wu, H. Tian and W. Zhu, *Angew. Chem., Int. Ed.*, 2019, **58**, 11593.

22 S. Ye, H. Rao, W. Yan, Y. Li, W. Sun, H. Peng, Z. Liu, Z. Bian, Y. Li and C. Huang, *Adv. Mater.*, 2016, **28**, 9648.

23 L. Calió, S. Kazim, M. Grätzel and S. Ahmad, *Angew. Chem., Int. Ed.*, 2016, **55**, 14522.

24 J. Shi, X. Xu, D. Li and Q. Meng, *Small*, 2015, **11**, 2472.

25 H. Elbohy, B. Bahrami, S. Mabrouk, K. M. Reza, A. Gurung, R. Pathak, M. Liang, Q. Qiao and K. Zhu, *Adv. Funct. Mater.*, 2019, **29**, 1806740.

26 S. Zhang, M. Stolterfoht, A. Armin, Q. Lin, F. Zu, J. Sobus, H. Jin, N. Koch, P. Meredith, P. L. Burn and D. Neher, *ACS Appl. Mater. Interfaces*, 2018, **10**, 21681.

27 J. H. Kim, P. Liang, S. T. Williams, N. Cho, C. C. Chueh, M. S. Glaz, D. S. Ginger and A. K. Y. Jen, *Adv. Mater.*, 2015, **27**, 695.

28 S. Sajid, A. M. Elseman, H. Huang, J. Ji, S. Dou, H. Jiang, X. Liu, D. Wei, P. Cui and M. Li, *Nano Energy*, 2018, **51**, 408.

29 X. Yin, P. Chen, M. Que, Y. Xing, W. Que and C. Niu, *ACS Nano*, 2016, **10**, 3630.

30 W. Chen, F. Liu, X. Feng, A. B. Djurišić, W. Chan and Z. He, *Adv. Energy Mater.*, 2017, **7**, 1700722.

31 J. R. Manders, S. W. Tsang, M. J. Hartel, T. Lai, S. Chen, C. M. Amb, J. R. Reynolds and F. So, *Adv. Funct. Mater.*, 2013, **23**, 2993.

32 H. Zhang, J. Cheng, F. Lin, H. He, J. Mao, K. S. Wong, A. K.-Y. Jen and W. C. H. Choy, *ACS Nano*, 2016, **10**, 1503.

33 W. Chen, Y. Wu, J. Liu, C. Qin, X. Yang, A. Islam, Y. Cheng and L. Han, *Energy Environ. Sci.*, 2015, **8**, 629.

34 H. Zhang, X. Ren, X. Chen, J. Mao, J. Cheng, Y. Zhao, Y. Liu, J. Milicc, W. Yin, M. Grätzelc and W. C. H. Choy, *Energy Environ. Sci.*, 2018, **11**, 2253.

35 W. Wu, P. N. Rudd, Z. Ni, C. H. V. Brackle, H. Wei, Q. Wang, B. R. Ecker, Y. Gao and J. Huang, *J. Am. Chem. Soc.*, 2020, **142**, 3989.

36 W. Yang, B. W. Park, E. H. Jung, N. J. Jeon, Y. C. Kim, D. U. Lee, S. S. Shin, J. W. Seo, E. K. Kim, J. H. Noh and S. I. Seok, *Science*, 2017, **356**, 1376–1379.

37 W. Chen, Y. Zhou, G. Chen, Y. Wu, B. Tu, F. Liu, L. Huang, A. M. C. Ng, A. B. Djurišić and Z. He, *Adv. Energy Mater.*, 2019, **9**, 1803872.

38 Z. Li, B. H. Jo, S. J. Hwang, T. H. Kim, S. Somasundaram, E. Kamaraj, J. Bang, T. K. Ahn, S. Park and H. J. Park, *Adv. Sci.*, 2019, **6**, 1802163.

39 J. E. Kim, S. S. Kim, C. Zuo, M. Gao, D. Vak and D. Y. Kim, *Adv. Funct. Mater.*, 2019, **29**, 1809194.

40 B. Dou, J. B. Whitaker, K. Bruening, D. T. Moore, L. M. Wheeler, J. Ryter, N. J. Breslin, J. J. Berry, S. M. Garner, F. S. Barnes, S. E. Shaheen, C. J. Tassone and K. Zhu, *ACS Energy Lett.*, 2018, **3**, 2558.

41 C. Gong, S. Tong, K. Huang, H. Li, H. Huang, J. Zhang and J. Yang, *Sol. RRL*, 2020, **4**, 1900204.

42 Q. Hu, H. Wu, J. Sun, D. Yan, Y. Gao and J. Yang, *Nanoscale*, 2016, **8**, 5350.

43 C. Zuo, D. Vaka, D. Angmoa, L. Ding and M. Gao, *Nano Energy*, 2018, **46**, 185.

44 X. Fan, W. Nie, H. Tsai, N. Wang, H. Huang, Y. Cheng, R. Wen, L. Ma, F. Yan and Y. Xia, *Adv. Sci.*, 2019, **6**, 1900813.

45 W. J. Scheideler, N. Rolston, O. Zhao, J. Zhang and R. H. Dauskardt, *Adv. Energy Mater.*, 2019, **9**, 1803600.

46 M. I. Saidaminov, J. Kim, A. Jain, R. Q-Bermudez, H. Tan, G. Long, F. Tan, A. Johnston, Y. Zhao, O. Voznyy and E. H. Sargent, *Nat. Energy*, 2018, **3**, 648.

This journal is © The Royal Society of Chemistry 2021

J. Mater. Chem. A, 2021, **9**, 5759–5768 | **5767**

47 D. Barboni and R. A. De Souza, *Energy Environ. Sci.*, 2018, **11**, 3266.

48 R. Islam, G. Chen, P. Ramesh, J. Suh, N. Fuchigami, D. Lee, K. A. Littau, K. Weiner, R. T. Collins and K. C. Saraswat, *ACS Appl. Mater. Interfaces*, 2017, **9**, 17201.

49 Z. Gao, Y. Wang, D. Ouyang, H. Liu, Z. Huang, J. Kim and W. C. H. Choy, *Small Methods*, 2020, **4**, 2000478.

50 Y. Zhao, H. Zhang, X. Ren, H. L. Zhu, Z. Huang, F. Ye, D. Ouyang, K. W. Cheah, A. K.-Y. Jen and W. C. H. Choy, *ACS Energy Lett.*, 2018, **3**, 2891.

51 F. Jiang, W. C. H. Choy, X. Li, D. Zhang and J. Cheng, *Adv. Mater.*, 2015, **27**, 2930.

52 L. Zhou, X. Guo, Z. Lin, J. Ma, J. Su, Z. Hu, C. Zhang, S. Frank Liu, J. Chang and Y. Hao, *Nano Energy*, 2019, **60**, 583.

53 I. J. Park, G. Kang, M. A. Park, J. S. Kim, S. W. Seo, D. H. Kim, K. Zhu, T. Park and J. Y. Kim, *ChemSusChem*, 2017, **10**, 2660.

54 F. Wang, H. Yu, H. Xu and N. Zhao, *Adv. Funct. Mater.*, 2014, **25**, 1120.

55 W. Li, W. Zhang, S. V. Reenen, R. J. Sutton, J. D. Fan, A. A. Haghighirad, M. B. Johnston, L. Wang and H. J. Snaith, *Energy Environ. Sci.*, 2016, **9**, 490–498.

56 H. Abdy, A. Aletayyeb, M. Kolahdouz and E. A. Soleimani, *AIP Adv.*, 2019, **9**, 015216.

57 F. Li, X. Deng, F. Qi, Z. Li, D. Liu, D. Shen, M. Qin, S. Wu, F. Lin, S. Jang, J. Zhang, X. Lu, D. Lei, C.-S. Lee, Z. Zhu and A. K.-Y. Jen, *J. Am. Chem. Soc.*, 2020, **142**, 20134–20142.

58 H. D. Kim, N. Yanagawa, A. Shimazaki, M. Endo, A. Wakamiya, H. Ohkita, H. Benten and S. Ito, *ACS Appl. Mater. Interfaces*, 2017, **9**, 19988.

59 G. -J. A. H. Wetzelaer, M. Scheepers, A. M. Sempere, C. Momblona, J. Ávila and H. J. Bolink, *Adv. Mater.*, 2015, **27**, 1837.

60 J. Bisquert and E. J. Juarez-Perez, *J. Phys. Chem. Lett.*, 2019, **10**, 5889.

5768 | *J. Mater. Chem. A*, 2021, **9**, 5759–5768

This journal is © The Royal Society of Chemistry 2021